Т. 89, № 1 **ЖУРНАЛ ПРИКЛАДНОЙ СПЕКТРОСКОПИИ** ЯНВАРЬ — ФЕВРАЛЬ 2022
V. 89, N 1 **JOURNAL OF APPLIED SPECTROSCOPY** JANUARY — FEBRUARY 2022

FLIGHT PARAMETER SETTING OF UNMANNED AERIAL VEHICLE HYPERSPECTRAL LOAD[**]

W. Tian [1,3], Q. Zhao [2,3]*, Y. Ma [2,3], X. Long [1,3], X. Wang [2,3]

[1] *College of Mechanical and Electrical Engineering, Shi Hezi University, Xinjiang, China*
[2] *College of Information Science and Technology, Shi Hezi University, Xinjiang, China*
[3] *Research Center for Space Information Engineering Technology, Xinjiang, China;*
e-mail: zqz_inf@shzu.edu.cn

Correct flight parameters are critical for obtaining high-quality unmanned aerial vehicle (UAV) remote sensing images. For the UAV, the Rikola hyperspectral load needs to set the instrument's exposure time, UAV flight mode, flight altitude, and other issues when acquiring data. Using the control variable method, UAV Rikola hyperspectral images were collected under different parameters, and the gray-scale target and image's quantitative evaluation index was used to obtain the spectral curves of gray-scale targets, ground features, signal-to-noise ratio (SNR), information entropy, and sharpness of imagery. The results of the comparative analysis show: the vegetation hyperspectral data quality was better when determining the Rikola hyperspectral exposure time using the 64% diffuse plate; UAV hover mode and cruise mode had little impact on data quality; when the flight altitude was within 100 m above ground level, the higher the flying height, the better the data quality. This study therefore provides evidence for obtaining high-quality data using UAV hyperspectral load.

Keywords: *unmanned aerial vehicle remote sensing, hyperspectral load, exposure time, flight mode, flight altitude.*

УСТАНОВКА ПАРАМЕТРОВ ГИПЕРСПЕКТРАЛЬНОЙ НАГРУЗКИ ДЛЯ БЕСПИЛОТНЫХ ЛЕТАТЕЛЬНЫХ АППАРАТОВ

W. Tian [1,3], Q. Zhao [2,3]*, Y. Ma [2,3], X. Long [1,3], X. Wang [2,3]

УДК 533.6

[1] *Колледж машиностроения и электротехники Университета Ши Хэцзы, Синьцзян, Китай*
[2] *Колледж информационных наук и технологий Университета Ши Хэцзы, Синьцзян, Китай*
[3] *Исследовательский центр космических информационных технологий,*
Синьцзян, Китай; e-mail: zqz_inf@shzu.edu.cn

(Поступила 19 сентября 2019, в окончательной редакции — 17 сентября 2020)

С использованием метода контрольных переменных получены гиперспектральные изображения беспилотных летательных аппаратов (БЛА) Rikola при различных параметрах. Для получения спектральных кривых полутоновых мишеней, наземных объектов, отношения сигнал/шум, информационной энтропии и резкости изображений использованы полутоновая мишень и количественная оценка качества изображения. Результаты сравнительного анализа показывают, что качество гиперспектральных данных о растительности лучше при определении времени гиперспектральной экспозиции Rikola с использованием 64% диффузной пластины, а режим зависания и круизный режим БЛА почти не влияют на качество данных. Показано, что при высоте полета в пределах 100 м над уровнем земли качество данных тем лучше, чем выше высота полета.

Ключевые слова: *дистанционное зондирование беспилотного летательного аппарата, гиперспектральная нагрузка, время экспозиции, режим полета, высота полета.*

[**] Full text is published in JAS V. 89, No. 1 (http://springer.com/journal/10812) and in electronic version of ZhPS V. 89, No. 1 (http://www.elibrary.ru/title_about.asp?id=7318; sales@elibrary.ru).

Introduction. In recent years, unmanned aerial vehicle (UAV) low-altitude remote sensing technologies have been widely developed in many fields and have become some of the most important technical means to obtain remote sensing data [1]. UAV flight platforms are low in cost, are easy to maintain, have few flight restrictions, are flexible in take-off and landing, and fly at low-altitude [2]. UAV hyperspectral imaging systems can obtain hyperspectral images with high spatial resolution, high spectral resolution, and high time resolution [3, 4]. However, when the hyperspectral load takes UAV as a platform to obtain data, it will involve setting some parameters, and these parameters have a significant impact on the quality of the remote sensing data. Therefore, finding the appropriate and relevant parameters is extremely important for obtaining high-quality remote sensing data.

Domestic and foreign scholars have already conducted research of the related parameter settings when using UAV as a platform to obtain remote sensing data. X. L. Hou et al. [5] used a method centered on the image's maximum local information entropy to obtain the best exposure value of the image. J. Y. Ning [6] discovered the optimal automatic exposure algorithm by studying the image information entropy and using the principle of instrument exposure. P. Walczykowski et al. [7] used a push-broom Headwa 11 MicroHyperspec A series' hyperspectral imager as the research object and compared UAV and other aviation systems to obtain the best sensor and flight parameters of the aerial remote sensing image data. This led them to determine the best exposure parameters of the hyperspectral scanning sensor. Y. Huang et al. [8] discussed the spectral characteristics and classification of hyperspectral data at different flight altitudes by rapidly identifying and studying high-spectral remote sensing images acquired by the UAV hyperspectral load at different altitudes. B. Liu [9] also analyzed the influence of image resolution on crop classification accuracy and classification efficiency at different flight altitudes. J. Lee et al. [10] used a SONY NEX-5N visible light camera as the research object and proposed a simple method for analyzing UAV image spatial resolution, evaluating the UAV image quality at different heights. Lastly, K. He [11] studied the influence of the attitude error of small UAV on the spatial spectral feature extraction by obtaining the attitude information of UAV. It can be seen that in previous researches, the majority scholars have studied the influence of unilateral factors on experimental results according to a specific application. These studies lack holistic consideration and comprehensive experimental verification analysis. Secondly, there is no relevant UAV hyperspectral experiment for comprehensive analysis of the imaging quality of the UAV frame-type hyperspectral imager.

We used a DJI M600 Pro UAV flight platform with a frame-type Rikola hyperspectral load, and considered the main setting parameters (exposure time, flight mode and flight altitude of the UAV) during data collection. By setting up contrast experiments, we analyzed the effects of these three main parameters on image quality. Additionally, using image quality evaluation indicators (SNR, information entropy, and sharpness) [12–14] we comprehensively analyzed the image quality under different parameters. Finally, this led us to discover the optimal flight parameters for obtaining the best image quality.

Materials and methods. The Rikola hyperspectral imager is a frame-type hyperspectral imager that can be used for both hand-held measurement and UAV. The performance parameters are shown in Table 1.

TABLE 1. Rikola Hyperspectral Performance Parameters

Parameter	Value
Field of view	36.5°
Focal length	9 mm
Wavelength	~500–910 nm
The number of Waveband	~0–380
The exposure time	~0.06–3000 ms
Spatial pixels	1010×1010

Figure 1 is a schematic diagram of the imaging principle of the Rikola hyperspectral instrument. The Rikola camera is a lightweight spectral camera based on the Fabry-Perot interferometer. It was developed by Finland's National Technology Research Center (VTT) [15]. The Rikola hyperspectral imager continuously captures images of different wavelengths, and these images of each frame are combined into a spectral data cube.

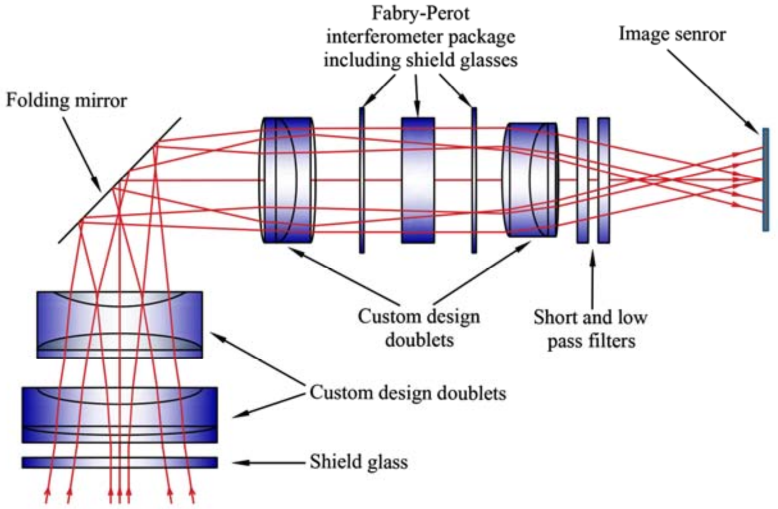

Fig. 1. Schematic diagram of the imaging principle of the Rikola hyperspectral instrument.

The Rikola hyperspectral imager uses a snapshot exposure method in which each waveband is continuously imaged at high speed in accordance with the exposure sequence. Image acquisition consists of exposure and reading, and the length of each data cube is equal to the sum of the exposure time and the storage time. The exposure time is to set according to the actual lighting conditions by using the diffuse plate before the hyperspectral imager/camera is set up on the UAV to perform the aerial photography task. The specific setting method is as follows.

The Rikola hyperspectral imager/camera was fixed on a camera tripod of about 1.5 m high. The diffuse plate was set up directly under the hyperspectral camera by moving the tripod.

The live imaging module of the Rikola Hyperspectral Imager software observes the gray histogram of the diffuse plate images obtained at this time. When the gray value was mainly distributed in the middle of the Gray histogram display panel, we recorded the exposure time displayed by the software. We assumed that this time recorded was the appropriate exposure time.

Data acquisition. The test area is located in a farmland within the 145th Regiment of Shihezi City, Xinjiang, China. The longitude and latitude are 85.957965 and 44.365951, respectively. Winter wheat is the main crop of the test area.

We used a DJI Matrice 600 Pro UAV (DJI, Shenzhen, China) flight platform. The Rikola hyperspectral instrument was carried on the UAV using a DJI Ronin-MX Pan-Tilt. In order to meet the requirements of image mosaic, all hyperspectral data were captured with an 80% along-track overlap and 75% side lap. The corresponding speeds of different flight altitudes and different flight modes are shown in Table 2.

TABLE 2. UAV Flight Speed at Different Flight Altitudes in Two Flight Modes

Flight mode	Flight speed, m/s			
	30 m AGL	50 m AGL	80 m AGL	100 m AGL
Cruise mode	4	4	4	4
Hover mode	2.4	4.1	6.5	

Data pre-processing. Firstly, we used the K-Type processing module in the Hyperspectral Imager software of the Rikola hyperspectral instrument to perform data format conversion and dark current correction on all original data. This allowed us to obtain the ENVI 5.3 general format and transform the data from the DN value (12bit: 0-4096) without physical units to the radiance value (the physical unit is W/[m^2·sr·nm]).

Secondly, we removed all hyperspectral data captured during the UAV flights' take off, descent and turning. We split the multi-band ENVI standard format data into a single-band.tif format data by using the Slplit HDR module in Coregistering software. Then we used the fast selection function of Agisoft Photoscan Professional software to eliminate useless data at take-off, landing, and turning points. The remaining, useful data was registered and mosaicked using Rikola hyperspectral RegMosaic software.

Finally, the mosaic data (radiance data) was put through ENVI 5.3 software in order to perform reflectance correction and obtain reflectance data. The reflectance data can be used for quantitative remote sensing research. The calibration model is

$$\text{Reflectance} = \frac{S_1 \times S_2}{S_3}, \tag{1}$$

where S_1 is the hyperspectral image radiation energy value; S_2 is the diffuse plate true reflectance; and S_3 is the diffuse plate radiation energy value.

In the experiment, the author used five diffuse plates (G8T Inc, Utah, USA) with reflectance values of 3, 22, 48, 64, and 99%; the true values of S_2 is shown in Fig. 2.

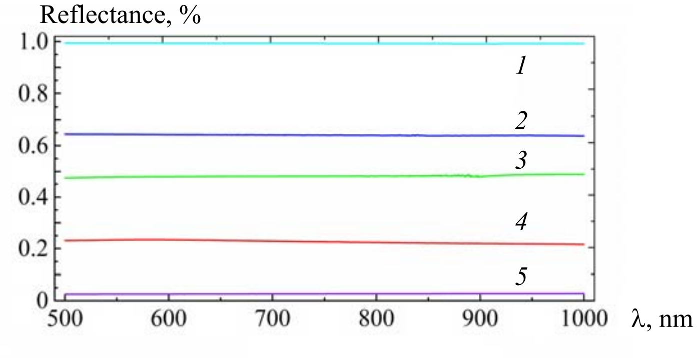

Fig. 2. Diffuse plates true reflectance curve, reflectance values of 99 (1), 64 (2), 48 (3), 22 (4), and 3% (5).

In order to compare the spectral curve changes of the diffuse plates under the six tests, we utilized the radiation correction method in Poncet's research [16], and thus this experiment uses a diffuse reflectance of 48% as a reference to obtain the hyperspectral reflectance data:

$$\text{Reflectance} = \frac{S_1 \times S_{2,48\%}}{S_{3,48\%}}, \tag{2}$$

where $S_{2,48\%}$ is the true reflectance of the 48% diffuse plate; $S_{3,48\%}$ is the radiation energy value of the 48% diffuse plate.

The acquisition of data by UAV Rikola hyperspectral imager/camera mainly involves captures of the exposure time, UAV flight mode, and flight altitude. First, on Apr. 6, 2018, the contrast test was designed with the UAV flight altitude and flight mode as variables. Under the same exposure time, hyperspectral data were collected at different flight altitudes in UAV cruise mode and hover mode so as to achieve a comparative analysis effect.

Next, on May 13, 2020, in cruise mode and at a fixed flight altitude of 80 m AGL, six test experiments were performed to assess the Rikola hyperspectral exposure time. The exposure times were obtained using 99, 64, 48, 22, and 3% diffuse plates with comprehensive reference to 99 and 64% diffuse plates.

Results and discussion. *Analysis of diffuse plates spectral curve to determine the exposure time.* As shown in Table 3, four control tests were established to assess the Rikola hyperspectral exposure time when using different diffuse reflector plates.

TABLE 3. Exposure Time under Different Parameters

Test	Diffuse plate, %	Exposure time, ms
Test I	99	3
Test II	99+64	4
Test III	64	5
Test IV	48	7
Test V	22	10
Test VI	3	15

Note. Flight amplitude 80 m AGL.

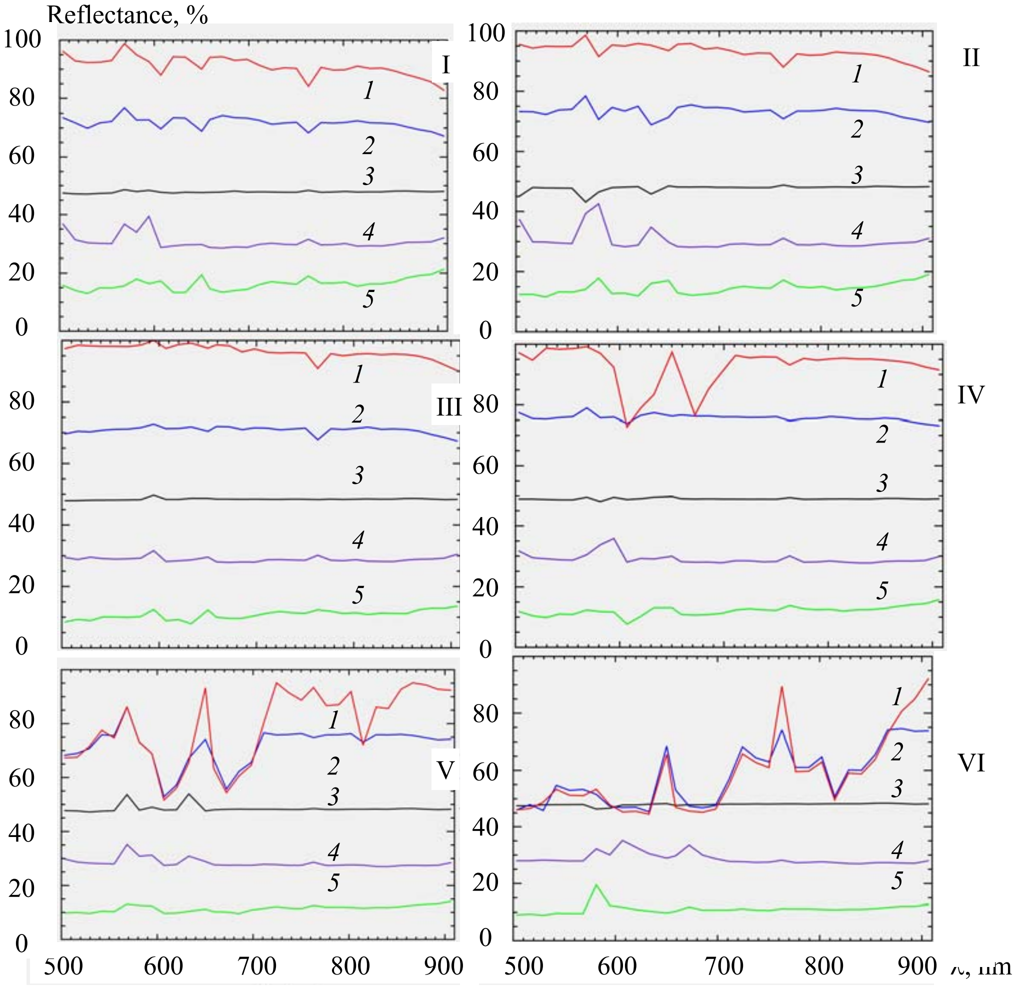

Fig. 3. The gray-scale target spectral curve of test I–VI: diffuse plate 99 (1), 64 (2), 48 (3), 22 (4), and 3% (5).

The data accuracy was higher when the relationship between the measured reflectance of the diffuse plates and the true reflectance was stronger [16]. When changing the exposure time, the measured reflectance curves of 3, 22, 64, and 99% diffuse plates were compared with the true reflectance, and all had different extent deviation (Fig. 3). In addition, when the exposure time was too long, overexposure occurred. This is demonstrated, for instance, by the distortion of the measured reflectance curves of 64 and 99% diffuse plates (test V and VI). Overall, when the exposure time is 5 ms, the deviation of the measured reflectance curve of the diffuse plates is the smallest, and therefore the measured reflectance of the diffuse plates is closest to the true reflectance (test III). Therefore, it is most accurate to determine the hyperspectral exposure time using the 64% diffuse plate.

Analysis of SNR results according to image quantitative evaluation index. The SNR of remote sensing images is a key indicator when evaluating the quality of data obtained by remote sensing sensors. The SNR of images can reflect the SNR performance of remote sensing instruments to a large extent. The common methods for evaluating SNR of remote sensing image include LMLSD, GS, EE-LMSD, and SSDC [17], among others. For hyperspectral images, the signal has a strong correlation between spectra or between wavebands. As such, linear regression was used to remove signals with hyperspectral correlation in the image, a process called decorrelation. This involves removing the signal with high correlation so that the remaining is noise [18]. In this paper, the SNR of the image was obtained using the space/spectral dimension correlation method (SSDC) which is highly reliable when compared to hyperspectral images.

Analysis of the noise characteristics of the instrument. First, we needed to analyze the noise characteristics in the Rikola hyperspectral system. The noise was mixed with the signal, and it was necessary to analyze whether there was correlation between the noise and the signal, and whether the noise itself had correlation.

(1) Analysis of correlation between noise and signal. The noise in the instrument can be divided into two main categories: additive noise and multiplicative noise [19]. The magnitude of the additive noise was not correlated with the signal, while the multiplicative noise was the opposite. The image was divided into 8×8 relatively uniform regions, and the mean and variance in each small region were calculated. As shown in Fig. 4, there was no obvious trend between the local mean and local variance. Therefore, it can be determined that the noise presence in the Rikola hyperspectral system is additive noise.

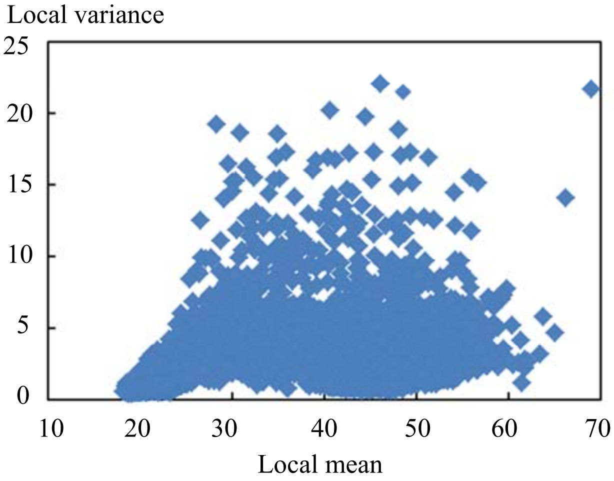

Fig. 4. Correlation diagram of signal and noise.

(2) Analysis of correlation between noise and noise. By removing the correlation of the signal in the spectral dimension from the Rikola data, the residual image can be used to determine the correlation of the noise itself. Figure 5 shows the correlation coefficient of the residual images. It can be seen that the noise in the Rikola hyperspectral signal was not correlated by itself.

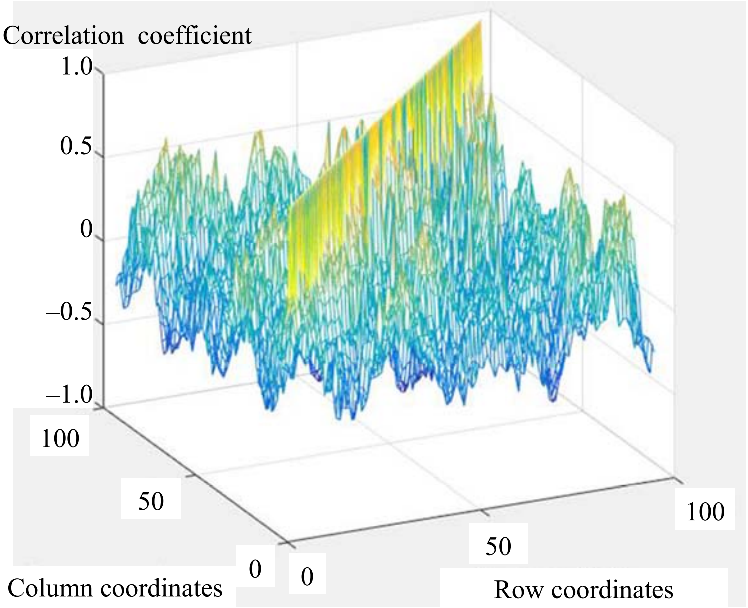

Fig. 5. Noise correlation coefficient.

Comparative analysis of image's SNR. The SSDC method uses a multiple linear regression method. The formula is as follows:

$$\hat{x}_{i,j,k} = ax_{i,j,k-1} + bx_{i,j,k+1} + cx_{p,k} + d \ . \tag{3}$$

The images were divided into many small blocks according to a certain size. $x_{i,j,k}$ is the image pixel's gray value of the k band, the i column, and the j line in a small block, $\hat{x}_{i,j,k}$ is the linear fitting value of an image grayscale, and a, b, c, and d are the linear regression coefficients used to minimize the sum of the squares of the residuals, where

$$x_{p,k}=\begin{cases} x_{i-1,j,k} & ,i>1,\\ x_{i,j-1,k} & ,i=1,j>1,\\ \text{Insignificance} & i=1,j=1.\end{cases} \tag{4}$$

The residual image after SSDC was

$$r_{i,j,k}=x_{i,j,k}-\hat{x}_{i,j,k}\,, \tag{5}$$

where $r_{i,j,k}$ was the residual value; there were

$$s^2=\sum_{1}^{w}\sum_{1}^{h}r^2_{i,j,k}\quad (i,j)\neq(1,1)\,, \tag{6}$$

in which w and h are the width and height of each small image.

The image noise variance is

$$\sigma_n^2 = s^2/(M-4), \tag{7}$$

$$M = w\times h - 1. \tag{8}$$

Using the SSDC method above to get the SNR, the relevant algorithm codes were written in Matlab 2018b, and this obtained the SNR diagram shown in Fig. 6.

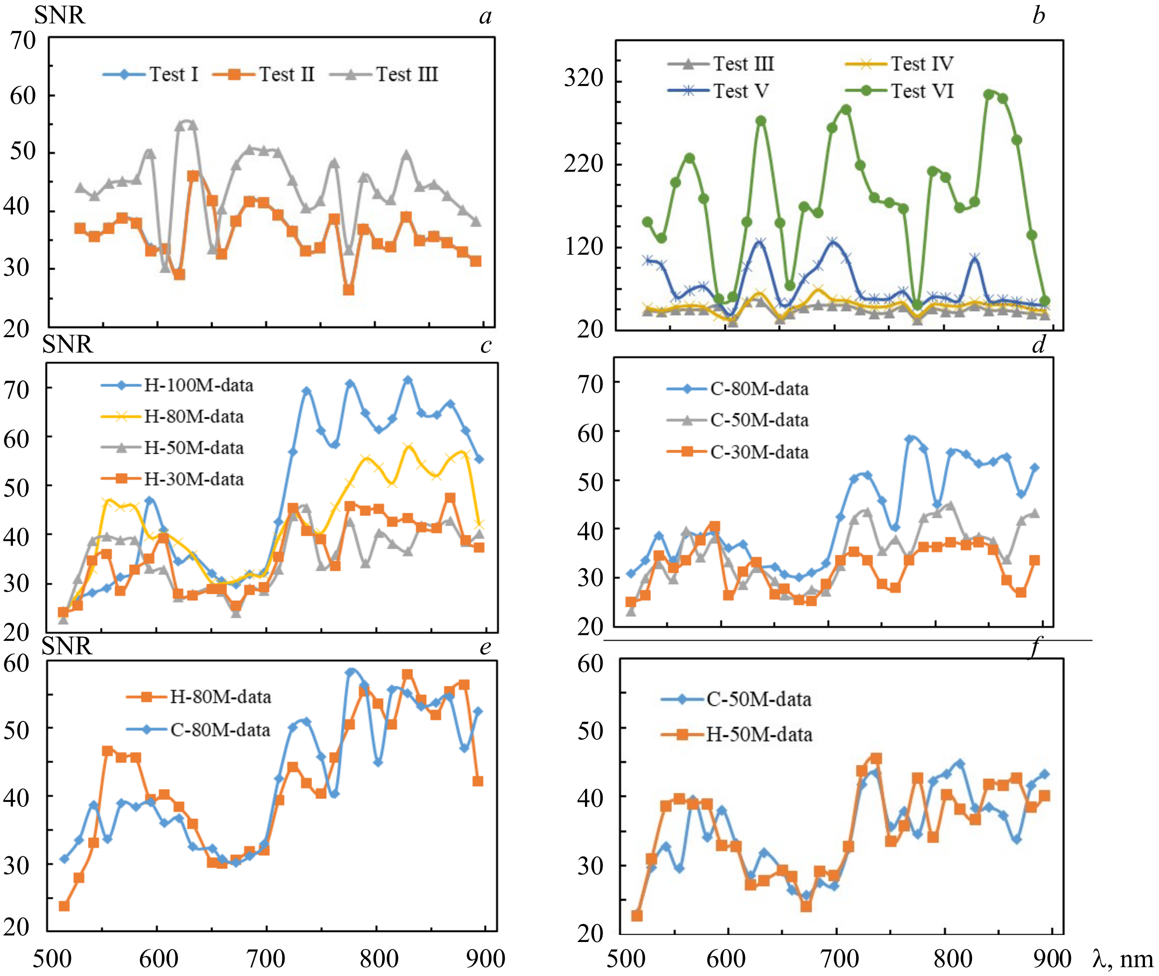

Fig. 6. Image SNR.

Figure 6a shows that as the exposure time of the hyperspectral camera increases, the SNR of the hyperspectral image becomes larger; but in tests I, II, III, IV, the SNR does not change significantly and is maintained at about 40. This result indicates that SNR of the image is maintained at a stable level as long as there is no overexposure. When the exposure time is too long (tests V, VI), the hyperspectral image is overexposed and the SNR of the hyperspectral image increases significantly. This is mainly because as the exposure time increases, the radiance value and the signal value become larger. The noise value remains unchanged, which leads to an increase in the numerator, a constant denominator, and therefore an increase in the ratio.

Figure 6b shows that in both hover and cruise modes, the SNR of the UAV hyperspectral images increases with the flight altitude, especially in the near-infrared band (~750–900 nm). At the same flight altitude (Fig. 6c), the SNR of the remote sensing images obtained by the hyperspectral UAV under the two flight modes was basically the same.

Analysis of information entropy results according to image quantitative evaluation index. Information entropy is a random measurement of the amount of information in an image, which reflects the degree of non-uniformity and complexity of the texture in the image. The large information entropy shows that all elements in the gray level co-occurrence matrix have maximum randomness. The more uniform the distribution of all element values in the matrix, the richer the image textures [20, 21]. The calculation formula is

$$ENT = -\sum_{i=1}^{n} p_x \log_2 p_x , \tag{9}$$

where P_x is the proportion of pixels with a gray value of x in the image.

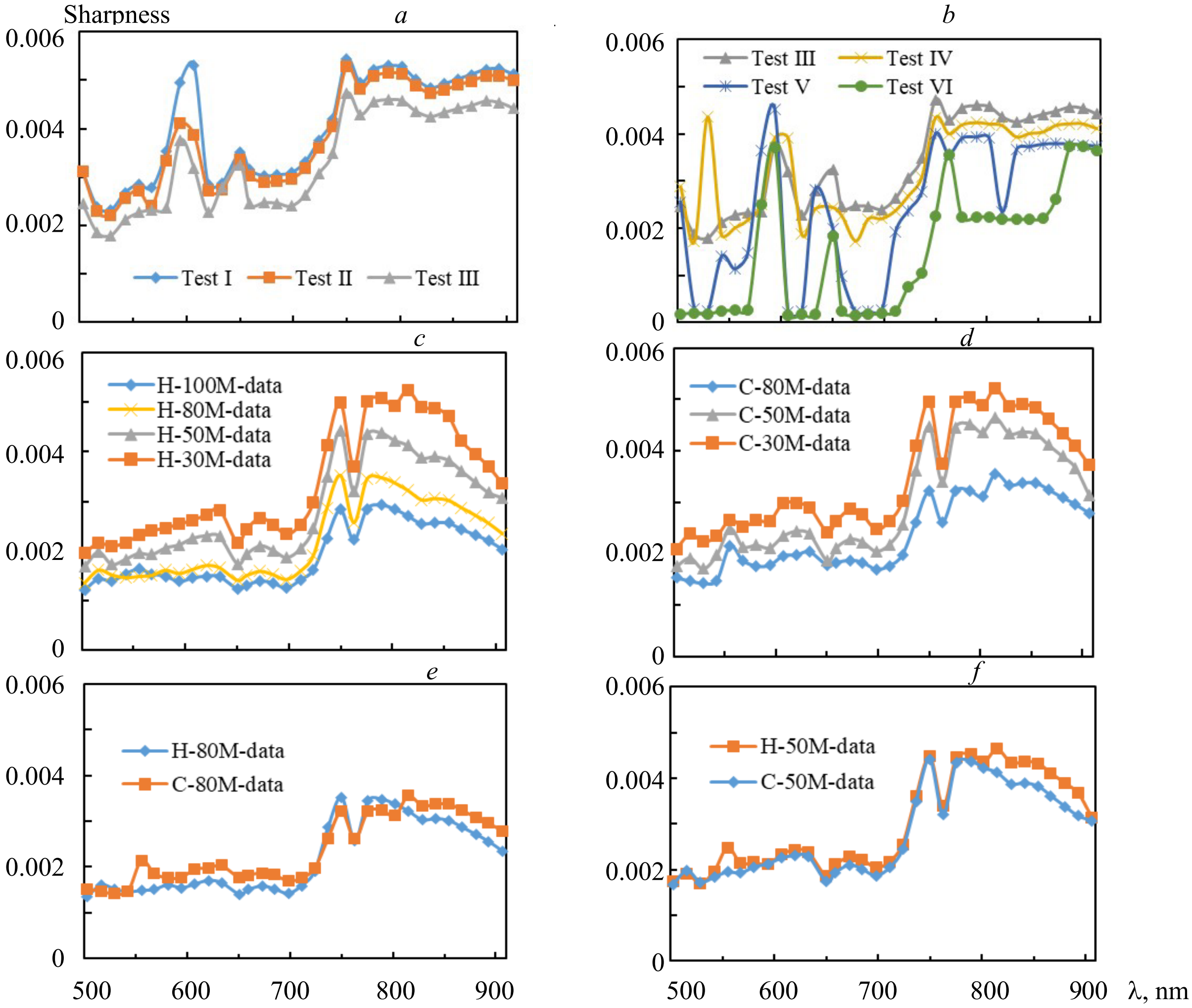

Fig. 7. Image sharpness.

Table 4 shows the results of image information entropy. The image information entropy of test III is higher than tests I, II, IV, V, VI). When the hyperspectral image is overexposed (tests V, VI), the information entropy of the hyperspectral image is greatly reduced. The overall overexposed image is brighter, so that the detailed texture information is overwhelmed, and the information entropy value is reduced. The information entropy of the hyperspectral image obtained by the UAV in cruise mode was slightly higher than that obtained by the UAV in hover mode. In both flight modes it can be seen that as the flight altitude of the UAV increases, the information entropy decreases slightly. For the winter wheat in the image, the texture distribution is uniform. When the flight altitude increases, meaning that the ground resolution of the hyperspectral image decreases and the texture complexity decreases, the information entropy decreases too.

Analysis of sharpness results according to image quantitative evaluation index. Sharpness refers to the degree of sharpness of the detailed shadows and their boundaries of the image, which is an important indicator reflecting the quality of remote sensing images. The sharpness of the image was calculated in this study using the average gradient method [22]. For the discrete image $x_{(i,j)}$, the first-order partial derivative can be expressed by a first-order difference approximation. The horizontal and vertical gradients at (i, j) were expressed as

$$g_i' = x_{(i,j+1)} - x_{(i,j)},$$
$$g_j' = x_{(i+1,j)} - x_{(i,j)}. \tag{10}$$

Gradient is a vector with the following value:

$$\mathrm{grad}_{(i,j)} = \frac{1}{(w-1)(h-1)} \times \sum_{i=1}^{w-1} \sum_{j=1}^{h-1} \sqrt{\frac{g_i'^2 + g_j'^2}{2}}, \tag{11}$$

where w and h are the width and height of each small image.

The gradient value was calculated for each pixel in the image. Then an average gradient of all the pixels in an image was taken in order to obtain the average gradient of the image. The Sobel operator used this method to calculate the sharpness index of each test image in MATLAB 2018b (Fig. 7). As shown in Fig. 7a, where there is no overexposure of the hyperspectral image (tests I, II, III, IV), when the exposure time of the hyperspectral camera increases, the sharpness of the hyperspectral image decreases. However, the sharpness does not change dramatically and remains at a stable level. When the hyperspectral image is overexposed (tests V, VI), the sharpness of the hyperspectral image is reduced, and large fluctuations occur in some of the bands, which means that the hyperspectral image is distorted. Figure 7b shows that whether the UAV acquires data in hover mode or cruise mode, its sharpness tends to drop with height. It is obvious that the higher the altitude, the lower the ground resolution of the image, which is to a certain extent the image clarity. However, it can be seen in this experiment that when flying at low altitude (about 100 m AGL), there is a low degree of change in clarity. Therefore, when acquiring hyperspectral data at low altitude, the main consideration is ground resolution, and the effect of sharpness on image quality can be ignored. Figure 7c shows that at the same flight altitude, the image sharpness under the two modes was similar at each height.

TABLE 4. Image Information Entropy

Data name	Information entropy
Test I	5.552680967
Test II	5.572480111
Test III	5.575306245
Test IV	5.560122301
Test V	2.793663644
Test VI	1.148716143
C-30M-data	5.874677524
C-50M-data	5.873981557
C-80M-data	5.873433867
H-30M-data	5.873278016
H-50M-data	5.870889858
H-80M-data	5.870088135
H-100M-data	5.869170854

Conclusions. By analyzing the spectral curve, SNR, information entropy, and image sharpness of hyperspectral data, we were able to draw several conclusions. Firstly, when conducting the research on objects such as vegetation, when the exposure value was set with reference to the 99% diffuse plate, the image may be overly dark. When the exposure value was set with reference to the 22 and 3% diffuse plate, the image may be overexposed. In contrast, when the exposure value was set with reference to the 64% diffuse plate, the image quality was relatively good. Secondly, flight mode (taking photos at equal intervals while hovering) had little effect on the image quality when there was a relatively small difference in flight speed between the two flight modes. Finally, the changes of information entropy and sharpness of hyperspectral images at different altitudes are on the order of one thousandth, so information entropy and sharpness cannot be used as a main basis for judging the quality of hyperspectral images of drones at different altitudes. However, it is noticed that the SNR of hyperspectral images at different altitudes changes obviously with altitude. Therefore, the comprehensive analysis of these three indicators shows that the higher the flying altitude, the better the overall quality of hyperspectral images.

Acknowledgments. The authors acknowledge financial support from Special Funding Projects for Local Science and Technology Development Guided by the Central Government (21610011) and Major Scientific and Technological Projects of the XPCC (2017DB005).

REFERENCES

1. H. Y. Cen, L. Wan, J. P. Zhu, *J. Plant Methods*, **15**, 1 (2019).
2. M. Li, Y. Q. Huang, X. M. Li, D. X. Peng, J. X. Xie, *J. Trans. Chin. Soc. Agric. Eng.*, **34**, No. 4, 108–114 (2018).
3. K. Uto, H. Seki, G. Saito, et al. *Workshop on Hyperspectral Image & Signal Processing: Evolution in Remote Sensing* (2017).
4. P. Mark, B. Dmitry, G. Kevin, K. J. Gaston, F. Gonzalez, *J. Sensors*, **18**, No. 7, 20–26 (2018).
5. X. L. Hou, H. B. Luo, P. P. Zhou, *J. Infrared Laser Eng.*, **46**, No. 7, 263–269 (2017).
6. J. Y. Ning, *The Research on Realization of the Auto-exposure Algorithm Based on Entropy, D. First Research Institute of China Aerospace Science and Technology Corporation*, 75–87 (2016).
7. P. Walczykowski, K. Siok, A. Jenerowicz, *J. Int. Arch. Photogrammetry, Remote Sensing Spatial Inform. Sci.*, **41**, 1065–1069 (2016).
8. Y. Huang, X. H. Chen, Y. L. Liu, Z. H. Huang, M. Sun, Y. C. Su, *J. Anhui Agric. Sci.*, **46**, No. 11, 170–173 (2018).
9. B. Liu, *Classification of Crops Based on UAV Remote Sensing Images, D. University of Chinese Academy of Sciences,* 29–44 (2019).
10. J. Lee, S. Sung, *J. Spatial Inform. Res.*, **24**, No. 2, 141–154 (2016).
11. K. He, *Research on Key Technologies of Aerial Remote Sensing System Based Small UAV, D. Chongqing University*, 15–32 (2017).
12. J. J. Yang, Y. Q. Zhao, C. Yi, J. C. W. Chan, *J. Remote Sens.*, **9**, No. 4, 305 (2017).
13. X. H. Cao, X. H. Li, Z. H. Li, L. C. Jiao, *Int. J. Remote Sens.*, **38**, No. 12, 3656–3668 (2017).
14. X. Y. Wang, J. Q. Li, J. Li, *J. IOP Conf. Ser. Mater. Sci. Eng.*, **466**, 12–53 (2018).
15. H. Saari, I. Pölönen, H. Salo, et al. *J. Proc. SPIE – The International Society for Optical Engineering*, **8889**, 6 (2013).
16. A. M. Poncet, K. Thorsten, B Christian, et al. *J. Remote Sens.*, **16**, 11 (2019).
17. B. Zhu, X. H. Wang, L. L. Tang, C. R. Li, *J. Remote Sens. Technol. Appl.*, **25**, No. 2, 303–309 (2010).
18. Q. Chen, Y. Q. Xue, *J. Remote Sens.*, **4**, 284–289 (2000).
19. B. R. Corner, *Int. J. Remote Sens.*, **24**, No. 4, 689–702 (2003).
20. D. Y. Tsai, Y. Lee, E Matsuyama, *J. Digital Imaging*, **21**, No. 3, 338–347 (2008).
21. H. Gao, Q. G. Miao, J. C. Yang, Z. X. Ma, *J. IEEE Access*, **99**, 1–5 (2018).
22. B. Y. Qin, R. Shang, S. Y. Li, B. Q. Hei, Z. W. Liu, *Reliable Sharpness Automatic-Evaluation Method for Optical Remote Sensing Images, C. Image Processing & Analysis* (2015).